Mechanical Su-Schrieffer-Heeger quasicrystal: Topology, localization, and mobility edge

D. A. Miranda [1], T. V. C. Antão [2], and N. M. R Peres [1,3,4]

[1]*Centro de Física (CF-UM-UP) and Departamento de Física, Universidade do Minho, P-4710-057 Braga, Portugal*
[2]*Department of Applied Physics, Aalto University, 02150 Espoo, Finland*
[3]*International Iberian Nanotechnology Laboratory (INL), Avenida Mestre José Veiga, 4715-330 Braga, Portugal*
[4]*POLIMA–Center for Polariton-driven Light-Matter Interactions, University of Southern Denmark,*
Campusvej 55, DK-5230 Odense M, Denmark

In this paper we discuss the topological transition between trivial and nontrivial phases of a quasiperiodic (Aubry-André like) mechanical Su-Schrieffer-Heeger model. We find that there exists a nontrivial boundary separating the two topological phases, and an analytical expression for this boundary is found. We discuss the localization of the vibrational modes using the calculation of the inverse participation ratio and access the localization nature of the states of the system. We find three different regimes: extended, localized, and critical, depending on the intensity of the Aubry-André spring. We further study the energy-dependent mobility edge (ME) separating localized from extended eigenstates and find its analytical expression for both commensurate and incommensurate modulation wavelengths, thus enlarging the library of models possessing analytical expressions for the ME. Our results extend previous results for the theory of fermionic topological insulators and localization theory in quantum matter to the classical realm.

I. INTRODUCTION

A real crystalline material always possesses some degree of disorder. Often, the disorder is of Anderson type [1,2], where a random potential is created by a finite concentration of impurities dispersed in the material. It is well know that in three dimensions, there exists a critical value of the potential intensity Δ above which a metal-insulator phase transition occurs [3]. In one dimension, however, all states are localized for any small but finite value of Δ, given the system is sufficiently large or in the thermodynamic limit. With the advent of twisted bilayer graphene [4–7] a new kind of disorder became easily accessible in condensed matter, dubbed quasiperiodic disorder. This comes about because, at certain twist angles, the electrons see a potential which is incommensurate with the lattice they propagate in, due to the presence of the second twisted layer. However, quasiperiodicity in electronic systems is not new, having a long tradition going back to studies by Aubry and André [8,9]. In their original paper, Aubry and André proposed a one-dimensional tight-binding model where electrons are subjected to a sinusoidal electrostatic potential incommensurate with the system's lattice. These two authors showed that a metal-insulator transition takes place for a finite value of $\Delta = 2t$, where t is the electronic hopping amplitude. All eigenmodes are either exponentially localized, if $\Delta > 2t$, or extended, if $\Delta < 2t$. This result is at odds with the case of Anderson localization in one-dimensional systems.

Together with metal-insulator transitions due to disorder, topological phase transitions in one and more dimensions [10] have also become a field of intense research. For example, robust quantum-state transfer in superconducting qubit chains via topologically protected edge states [11] was experimentally realized and quantum-information processing via chiral

Majorana edge modes in Kitaev materials [12] was proposed. In any spatial dimension, and in the absence of disorder, such phase transitions are abrupt, as the system suddenly jumps from a trivial phase, hosting no edge states, to a topological one hosting edge states. Thus, in the latter case, an electronic system supports dissipationless charge transport due to chiral edge states (for an adiabatic cyclic evolution of the Hamiltonian we have, for example, the Thouless pumping in 1D [13]) carried by integer or fractional charge excitations [14]. A natural question now arises on the interplay between topology and quasiperiodic disorder.

The Su-Schrieffer-Heeger (SSH) model is the ideal platform for investigating the aforementioned interplay. In brief, the SSH model is described by the tight-binding equations [15]

$$t\psi_{j-1}^{B} + v\psi_{j}^{B} = E\psi_{j}^{A},$$
$$t\psi_{j+1}^{A} + v\psi_{j}^{A} = E\psi_{j}^{B}, \qquad (1)$$

where t, v are two hopping amplitudes that connect lattice sites labeled by the index j and the sublattice index A/B. It is the simplest one-dimensional model with topological features, possessing two topological phases characterized by winding numbers $\nu = 0$ and $\nu = 1$, the latter being topologically nontrivial and supporting edge states, eigenstates that are localized at the boundaries of the system. The existence (or absence) of edge states can also be predicted through the bulk-boundary correspondence [16,17]. In fact, it is possible for variations of this model to host more than one edge state per edge, by introducing long-range hoppings and inducing a nonequilibrium steady state across the chain, for example [18]. The topological phases of the SSH model can be seen as a consequence of its underlying symmetries,

like chiral, parity, time-reversal, and particle-hole symmetries [19]. This is true even for a non-Hermitian variant of the model [20], with more exotic symmetries like anti-PT symmetry. Recently, studies have shown that random chiral-preserving [18,21], chiral-breaking [18,22], and quasiperiodic intracell hopping modulation [23] can induce topological phase transitions on SSH-based systems, that would not occur otherwise. Indeed, in a previous study [24], we have showcased how quasiperiodicity can induce complex features in the topological description of the SSH model. In such a system, quasiperiodic modulation of intra- and intercell hoppings can enable the coexistence of topological edge modes linked to 1D and 2D topological invariants. Additionally, when this model is subjected to quasiperiodicity, nontrivial localization phenomena, not present in the original Aubry-André (A-A) model, arise, such as the existence of energy-dependent mobility edges (MEs), and critical phases for multiple values of disorder strength [23,25,26] appear.

As noted above, Aubry and André studied Anderson localization in a 1D tight-binding model whose disorder applied to a periodic lattice was of sinusoidal form. The model is described by

$$t(\psi_{j+1} + \psi_{j-1}) + \Delta\cos(2\pi\beta j + \phi)\psi_j = E\psi_j, \quad (2)$$

where j is the lattice index, Δ is the strength of the quasiperiodic potential, t is the hopping amplitude between neighboring sites, ϕ is the phase parameter, and β is an irrational number [8]. This model is the simplest model concerning quasiperiodicity in which quasidisorder can induce abrupt metal-insulator transitions: all eigenmodes are either exponentially localized if $\Delta > 2t$ or extended plane waves if $\Delta > 2t$. At the condition $\Delta = 2t$, the A-A model is said to possess self-duality, meaning that the Hamiltonian both in real and momentum spaces has the same identical form. From there, different quasiperiodic models have been introduced and understood theoretically [26–28] and experimentally realized [29–31]. One notable property of the original A-A model is that the boundary separating the extended and localized phases is energy independent. Thus, no energy-dependent mobility edge (ME) (energy value that marks the boundary between localized and extended states [32,33]) can exist in this model, unlike in 3D random disordered systems, for example [2,34]. This is a peculiarity of the Aubry-André model, since, in general, generalized versions of this model possess energy-dependent MEs [35,36]. Indeed, it was already shown before that 1D quasiperiodic models can host energy-dependent MEs by introducing long-range hopping amplitudes to the base lattice [27] or by applying some variation of the A-A potential to the Su-Schrieffer-Heeger model [23,25,26].

In this work, inspired by recent studies of SSH-based models in classical wave systems, like elastic [21,37–41], photonic [42,43], acoustic [44–46], and superconducting systems [47–49], and by exciting localization phenomena induced by quasiperiodicity [26,35,36], we investigate a mechanical version of the SSH model subjected to an A-A intercell spring constant. We focus on the limit where only the intercell elastic spring constant is altered by the A-A modulation. That is, the intracell elastic constant (between masses u_A^j, u_B^j) remains fixed, whereas the inter-unit-cell elas-
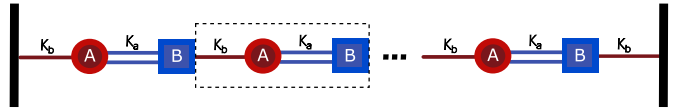

FIG. 1. Depiction of the mechanical SSH with fixed boundary conditions. The dashed rectangle contains one unit cell.

tic constant (between u_A^{j+1}, u_B^j) is allowed to vary. We study the 1D topological phases of the chiral version of this model numerically and analytically, in order to understand how variations in the strength, periodicity, and relative shift of the A-A potential affect the topological phases and correspondent winding numbers. Then, we make use of the inverse participation ratio (IPR) and the fractal dimension to study the localization properties of both chiral and nonchiral versions of our model. Finally, the equivalent of mobility edges for our mechanical system is derived analytically for the nonchiral system based on Avila's global theory [50].

This paper is organized as follows. In Sec. II we introduce the mechanical SSH model, without yet considering quasiperiodicity, and discuss the topological properties of our classical mechanical model as a function of the ratio between spring constants and the intensity of the intercell spring modulation. In Sec. III we discuss the effect of A-A modulation on the winding number phase diagram and on the localization of the eigenstates. Next, we derive an analytical expression of the energy-dependent mobility edge. Finally, we offer our conclusions and detail some of the calculations in the appendices.

II. MECHANICAL SSH CRYSTAL

In this section, we introduce our SSH mechanical model (see Fig. 1), define the notation, and discuss the model topological properties from a real-space perspective.

A. Model and notation

The system is a finite 1D chain subjected to fixed boundary conditions (FBCs), composed of N unit cells with two equal masses m each. Each mass carries with itself two labels: the sublattice index $\alpha = \{A, B\}$ and the cell index $j \in [1, N]$. Additionally, two spring constants are defined: the intracell spring K_a and the intercell spring K_b. These spring constants correspond to the hopping amplitudes in the original electronic SSH model and, as will be shown later, tuning their values can lead to different topological phases in the mechanical model. The equations of motion obeyed by a mass of the type A and a mass of the type B are obtained from the Euler-Lagrange method and can be represented in matrix form as

$$\ddot{\mathbf{U}}(t) = -\mathbb{M}U(t), \quad (3)$$

where $U(t) = [u_A^1, u_B^1, u_A^2, u_B^2, \dots, u_A^N, u_B^N]$ is the displacement vector, and $u_\alpha^j(t)$ is the displacement of the mass j with sublattice label $\alpha = A/B$. Since the normal modes have a well-defined frequency, we can separate the temporal and spatial parts. This allows us to write $\ddot{u}_\alpha^j$ in terms of u_α^j as
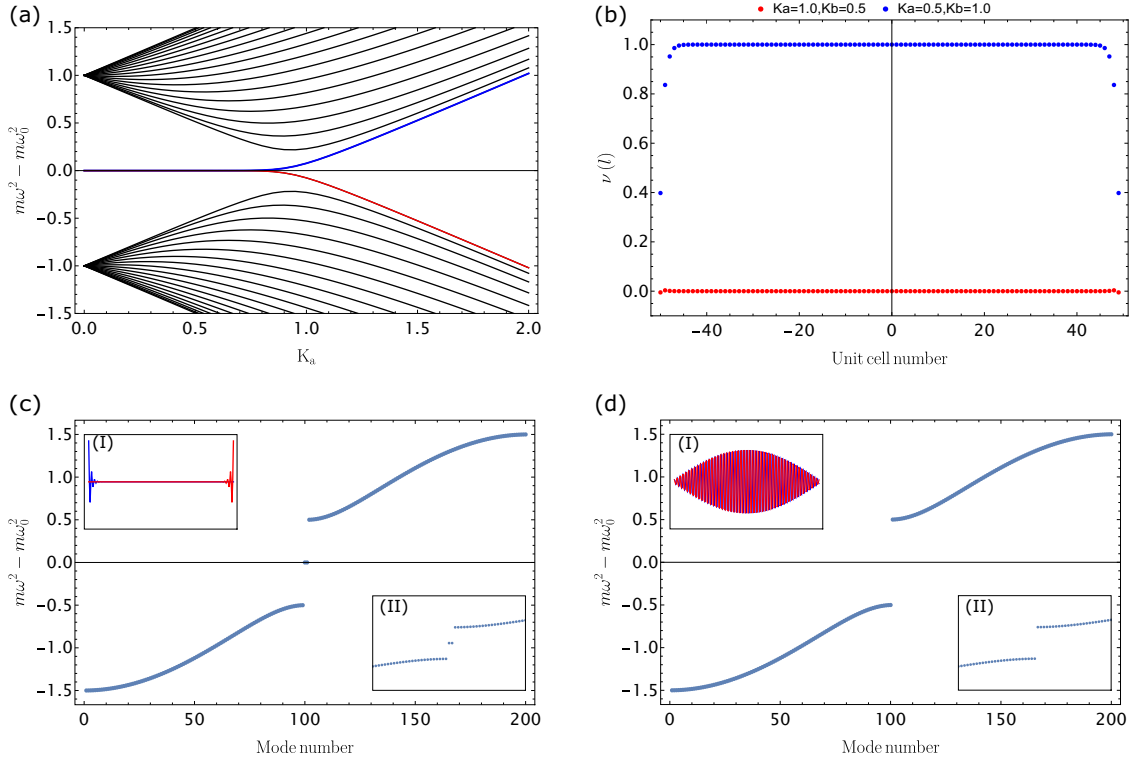
FIG. 2. (a) Evolution of the eigenvalue spectrum of $\mathbb{M}' = (\mathbb{M} - m\omega_0^2 \mathbb{I})$ for $K_b = 1$, $m = 1$. The edge states, depicted in red and blue, are zero-energy states for $K_a < K_b$ and become bulk states for $K_b < K_a$. (b) LTMs calculated for $K_a = 1$, $K_b = 0.5$ (red curve) and $K_a = 0.5$, $K_b = 1$ (blue curve). For unit cells distant from the borders, the LTMs $\nu(j)$ converge to the winding number $\nu = 0, 1$. (c) Eigenvalue spectrum of $\mathbb{M}'$ for $K_b = 1$, $K_a = 0.5$. (c) (I) Eigenmodes number 100 and number 101 are localized at the borders and are thus labeled edge states. (c) (II) Edge states are degenerate and are present in the middle of the gap. (d) Eigenvalue spectrum of $\mathbb{M}'$ for $K_b = 0.5$, $K_a = 1$. (d) (I) Eigenmodes number 100 and number 101 are now delocalized. (d) (II) For this configuration there are no edge states. Instead, these eigenmodes are extended states.

follows:

$$u_\alpha^j(t) = C_{\alpha,j} e^{-i\omega t} \rightarrow \ddot{u}_\alpha^j(t) = -\omega^2 u_\alpha^j(t), \qquad (4)$$

so the equations of motion reduce to the following eigenvalue problem:

$$\mathbb{M} U(t) = m\omega^2 U(t), \qquad (5)$$

where $\mathbb{M}$ is the dynamical matrix of dimension $2N \times 2N$. It has the form

$$\mathbb{M} = \begin{bmatrix} K_a + K_b & -K_a & 0 & \ldots & 0 \\ -K_a & K_a + K_b & -K_b & \ldots & 0 \\ 0 & -K_b & K_a + K_b & \ldots & 0 \\ \ldots & \ldots & \ldots & \ldots & -K_a \\ 0 & 0 & 0 & \ldots K_a + K_b \end{bmatrix}_{2N \times 2N}. \quad (6)$$

Differently from the original SSH model Hamiltonian, the mechanical spring-mass dynamical matrix $\mathbb{M}$ has elements in its diagonal. However, since all diagonal elements are equal, the system still possesses chiral symmetry, as the diagonal elements represent only a shift in the eigenvalue spectrum of the form $m\omega_0^2 = K_a + K_b$. Then, we can define the matrix $\mathbb{M}' = (\mathbb{M} - m\omega_0^2 \mathbb{I})$ that obeys an anticommutation relation with the chiral operator Γ, and whose eigenvalue spectrum is centered around $m\omega^2 = 0$,

$$\Gamma(\mathbb{M} - m\omega_0^2 \mathbb{I}) + (\mathbb{M} - m\omega_0^2 \mathbb{I})\Gamma = 0,$$

where $\mathbb{I}$ is the $2N \times 2N$ identity matrix, and Γ is the chiral operator, whose matrix representation for the FBC spring-mass system is

$$\Gamma = \begin{bmatrix} 1 & 0 & 0 & 0 & \ldots \\ 0 & -1 & 0 & 0 & \ldots \\ 0 & 0 & 1 & 0 & \ldots \\ 0 & 0 & 0 & -1 & \ldots \\ \vdots & \vdots & \vdots & \vdots & \ddots \end{bmatrix}_{2N \times 2N}. \quad (7)$$

The mechanical SSH eigenvalue spectrum is represented in Figs. 2(c) and 2(d), each corresponding to one different topological phase, which will be discussed next.

B. Topological characterization in real space

For very large systems, translation symmetry is exact in the bulk (this is not the case near the system's terminations). Due to this property, it is possible to define topological markers in real space [21,51,52], which allows us to discriminate between topologically trivial and topologically nontrivial phases in nonperiodic systems. In the present work we only consider systems that do not possess translation symmetry. The usual winding number computation in momentum space for periodic systems [41] must therefore be handled in real space. For this purpose we use the concept of a local topological marker (LTM) as defined in [51]. A LTM has a local value for each unit cell and, when averaged away from the border, it

converges to the winding number of the periodic system. The advantage of the LTM is that it can also deal with disordered systems [21,51,52]. To compute the LTMs for a chain with N unit cells, a $2N \times 2N$ matrix $\mathbb{U} = [U_1, U_2, U_3, \ldots, U_{2N}]$ is constructed, whose columns are normalized eigenvectors of the system in ascending order (the first column is then the eigenvector corresponding to the smallest eigenvalue). $\mathbb{U}$ can be divided in two: $\mathbb{U}_- = [U_1, U_2, U_3, \ldots, U_N]$ containing the first half eigenvectors below band gap at zero energy and $\mathbb{U}_+ = [U_{N+1}, U_{N+2}, U_{N+3}, \ldots, U_{2N}]$ containing the eigenvectors above the band gap at zero energy. With $\mathbb{U}_+$ and $\mathbb{U}_-$ we can construct the projectors of the bands above and below the gap: $\mathbb{P}_+ = \mathbb{U}_+ \mathbb{U}_+^T$ and $\mathbb{P}_- = \mathbb{U}_- \mathbb{U}_-^T$, respectively. The flat-band Hamiltonian, which is homotopically equivalent to $\mathbb{M}$ [52], is defined as $\mathbb{Q} = \mathbb{P}_+ - \mathbb{P}_-$, which can be decomposed as $\mathbb{Q} = \mathbb{Q}_{AB} + \mathbb{Q}_{BA} = \Gamma_A \mathbb{Q} \Gamma_B + \Gamma_B \mathbb{Q} \Gamma_A$, where

$$\Gamma_A = \begin{bmatrix} 1 & 0 & 0 & 0 & \ldots \\ 0 & 0 & 0 & 0 & \ldots \\ 0 & 0 & 1 & 0 & \ldots \\ 0 & 0 & 0 & 0 & \ldots \\ \vdots & \vdots & \vdots & \vdots & \ddots \end{bmatrix}_{2N \times 2N},$$

$$\Gamma_B = \begin{bmatrix} 0 & 0 & 0 & 0 & \ldots \\ 0 & 1 & 0 & 0 & \ldots \\ 0 & 0 & 0 & 0 & \ldots \\ 0 & 0 & 0 & 1 & \ldots \\ \vdots & \vdots & \vdots & \vdots & \ddots \end{bmatrix}_{2N \times 2N} \quad (8)$$

are the sublattice projectors and $\Gamma = \Gamma_A - \Gamma_B$ is the chiral operator. Finally, the definition of LTM according to Ref. [51] is

$$\nu(j) = \frac{1}{2} \sum_{\alpha=A,B} \{ (\mathbb{Q}_{BA}[\mathbb{X}, \mathbb{Q}_{AB}])_{j\alpha, j\alpha} + (\mathbb{Q}_{AB}[\mathbb{Q}_{BA}, \mathbb{X}])_{j\alpha, j\alpha} \}, \quad (9)$$

where $\mathbb{X}$ is the position operator with dimensions $\dim(\mathbb{X}) = 2N \times 2N$, in which the masses are mapped to the position of their unit cell counting from the center of the system: $\mathbb{X} = \text{diag}[-N, -N, -(N-1), -(N-1), \ldots, N-1, N-1]$, where the symbol diag[...] stands for a diagonal matrix.

The subindexes jA, jB indicate the entries for a mass of type A or B of the jth unit cell in the matrix. The average of the LTM $\nu(j)$ over the most central cells results in the quantity $\langle \nu \rangle$ that converges to the winding number ν of the system which, in this model, can have two values: $\nu = 0, 1$, characterizing the topologically trivial and nontrivial phases, respectively. Each phase corresponds to a specific ratio between K_a and K_b as we show in Figs. 2(a) and 2(b) ($\frac{K_a}{K_b} > 1$ corresponds to the trivial phase, while $\frac{K_b}{K_a} > 1$ corresponds to the topological phase). Additionally, in the topological phase with $\nu = 1$, the system possesses edge states (or rather, end states). They are not present if $\nu = 0$ or if we have periodic boundary conditions. This property is depicted in Figs. 2(c) and 2(d), where the energy spectrum and the shape of the edge states, if there are any, can be seen side by side.
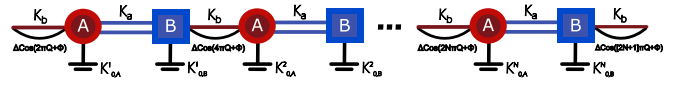

FIG. 3. Depiction of the mechanical SSH subjected to an Aubry-André modulation on the intercell spring constants. In order to preserve chiral symmetry, a local spring is added in each mass. It depends on the mass type and on the unit cell it is in.

III. MECHANICAL MODEL WITH INTERCELL AUBRY-ANDRÉ SPRING CONSTANTS

In this section we discuss the topological properties, localization, and energy-dependent mobility edges of our mechanical SSH model.

A. Equations of motion

We begin by studying a nearest-neighbor mechanical model under influence of an Aubry-André modulation (see Fig. 3). This modulation is characterized by a sinusoidal term whose wavelength is incommensurate with the lattice, due to the irrational number Q, chosen here to be the inverse of the golden ratio $\tau^{-1} = \frac{2}{1+\sqrt{5}}$. Here, we are interested in studying how the induced quasidisorder imposed by the A-A modulation affects the topological properties of the system, using the local topological marker formalism discussed above. In our model, the A-A is manifested as a perturbation on the spring values, rather than an additional local spring attached to each mass (this would characterize an on-site A-A potential). This means that the values of the spring constants change due to the A-A term. In our model, we apply the Aubry-André modulation only to intercell spring constants, K_b, that connects the masses u_A^{j+1} and u_B^j. Thus, the equations of motion for a unit cell j are as follows (time dependence implicit):

$$m\ddot{u}_A^j = -[K_a + K_b + \Delta\cos(2\pi Q j + \phi)]u_A^j + K_a u_B^j + [K_b + \Delta\cos(2\pi Q j + \phi)]u_B^{j-1},$$

$$m\ddot{u}_B^j = -\{K_a + K_b + \Delta\cos(2\pi Q[j+1] + \phi)\}u_B^j + K_a u_A^j + \{K_b + \Delta\cos(2\pi Q[j+1] + \phi)\}u_A^{j+1}, \quad (10)$$

where Δ is the A-A amplitude and $j \in [1, N]$ is the unit cell index. A perturbation on the springs also introduces a term in the diagonal (this does not happen in the original SSH model), implying that an off-diagonal A-A potential changes both diagonal and off-diagonal terms, breaking chiral symmetry. To avoid this, we add local springs $K_{0,\alpha}^j$ to each mass,

$$m\ddot{u}_A^j = -[K_a + K_b + \Delta\cos(2\pi Q j + \phi) + K_{0,A}^j]u_A^j + K_a u_B^j + [K_b + \Delta\cos(2\pi Q j + \phi)]u_B^{j-1},$$

$$m\ddot{u}_B^j = -\{K_a + K_b + \Delta\cos(2\pi Q[j+1] + \phi) + K_{0,B}^j\}u_B^j + K_a u_A^j + \{K_b + \Delta\cos(2\pi Q[j+1] + \phi)\}u_A^{j+1}, \quad (11)$$

with $K_{0,A}^j = \Delta[1 - \cos(2\pi Q j + \phi)]$ and $K_{0,B}^j = \Delta\{1 - \cos(2\pi Q[j+1] + \phi)\}$.

This choice of $K_{0,A}^j$ and $K_{0,B}^j$ preserves the chirality of the dynamical matrix and allows the computation of a quantized topological marker $\langle \nu \rangle$. Additionally, this choice guarantees

that the eigenvalues of the problem are always positive. Normal modes, which, by definition, have well-defined frequency, obey $\ddot{u}^j_\alpha(t) = -\omega^2 u^j_\alpha(t)$ and Eq. (10) becomes

$$m\omega^2 u^j_A = (K_a + K_b + \Delta)u^j_A - K_a u^j_B - [K_b + \Delta\cos(2\pi Qj + \phi)]u^{j-1}_B,$$

$$m\omega^2 u^j_B = (K_a + K_b + \Delta)u^j_B - K_a u^j_A - \{K_b + \Delta\cos(2\pi Q[j+1] + \phi)\}u^{j+1}_A, \tag{12}$$

or in matrix form

$$\mathbb{M} = \begin{bmatrix} K_a + K_b + \Delta & -K_a & 0 & \dots & -[K_b + \Delta\cos(2\pi Q + \phi)] \\ -K_a & K_a + K_b + \Delta & -[K_b + \Delta\cos(4\pi Q + \phi)] & \dots & 0 \\ 0 & -[K_b + \Delta\cos(4\pi Q + \phi)] & K_a + K_b + \Delta & \dots & 0 \\ \dots & \dots & \dots & \dots & -K_a \\ -[K_b + \Delta\cos(2\pi Q + \phi)] & 0 & 0 & \dots & K_a + K_b + \Delta \end{bmatrix}_{2N \times 2N} . \tag{13}$$

One important aspect to note is that true quasiperiodicity can only be achieved in infinite systems, in which the quasiperiodic perturbation never repeats itself. Numerically, one can only approximate true quasiperiodicity and its properties by working with sufficiently large systems. However, we aim to perform finite size scaling analysis and are thus forced to work with different system sizes. In this scenario, it is necessary to mimic an infinite-sized chain by imposing periodic boundary conditions (PBCs) in the original crystal lattice and defining the appropriate rational approximant, as detailed in Appendix A, on the additional A-A potential. This guarantees that the whole system is composed of only one unit cell, in the sense that the A-A potential never repeats itself throughout the finite system. Thus, from now on, PBCs are always imposed.

B. Topological characterization in the incommensurate regime

We begin our discussion of the topological phase as a function of varying K_a and Δ for fixed K_b. For each combination of parameters K_a and Δ, we calculate the quantity $\langle \nu \rangle$ as described in Sec. I B, which converges to the winding number. Figure 4 shows the corresponding phase diagram for $K_b = 2$, $\phi = 0$, rational approximant $\tilde{Q} = 377/610$, $N = 610$ unit cells, $K_a \in [0, 4]$, and $\Delta \in [0, 6]$. As expected from the original SSH model ($\Delta = 0$), the topological phase transition occurs for $K_a = K_b$ [16]. As Δ increases from 0 to 2, the trivial topological phase becomes available for $K_a < K_b$ due to the quasiperiodic disorder. For $\Delta > K_b = 2$, we see that the boundary between the two phases becomes linear and the phase diagram acquires a reentrant behavior. In the limit of very large Δ, the system becomes unable to access the topological phase, as the intracell spring becomes much greater than the intercell spring and the chain converges to a fully dimerized limit, as if there were no intercell springs.

Next, we study the behavior of the localization length. It is well known [52–54] that in electronic systems the topological phase transitions are accompanied by a divergence of the localization length at the Fermi level. This coincides with the closing of the band gap. To confirm that this general statement is also valid for our mechanical model, the localization length Λ was calculated analytically and verified

to diverge in the region between topological phases, where the gap closes. In order to simplify the calculation, we center the eigenvalue spectrum in zero by subtracting $m\omega_0^2 = K_a + K_b + \Delta$ from each eigenvalue, such that the states in the middle of the spectrum become zero-energy states when the gap closes, that is, $m\omega^2 - m\omega_0^2 = 0$. Then, the equations of motion for states with zero energy when the gap closes

FIG. 4. Averaged LTMs calculated for the spring-mass system with Aubry-André modulation applied on the intercell spring constant for $K_b = 2$, $\phi = 0$, and $m = 1$. The blue region corresponds to the trivial phase with $\langle \nu \rangle = 0$ and the red region corresponds to the topological phase $\langle \nu \rangle = 1$. Between the two phases, the white stripe separates the two phases and corresponds to a set of points where the averaged LTM did not converge to either 0 or 1 due to the finite system size. The black line is the analytical result for where the localization length diverges. The agreement between the white and black stripes is a manifestation of the fact that the topological phase transition is accompanied by a divergent localization length.

read

$$
0 = K_a u_B^j + [K_b + \Delta \cos(2\pi Q j + \phi)]u_B^{j-1},
$$
$$
0 = K_a u_A^j + \{K_b + \Delta \cos(2\pi Q[j+1] + \phi)\}u_A^{j+1}. \quad (14)
$$

Now, each equation only has coefficients of the same sublattice. The equation with sublattice A coefficients, for example, and can be written as

$$
u_A^{j+1} = \frac{-K_a}{K_b + \Delta \cos(2\pi Q[j+1] + \phi)} u_A^j, \quad (15)
$$

which leads to a recursive relation

$$
u_A^N = (-1)^{N-1} \prod_{j=1}^{N-1} \frac{K_a}{K_b + \Delta \cos(2\pi Q[j+1] + \phi)} u_A^1. \quad (16)
$$

Now, the relevant Lyapunov exponent γ, the inverse of the localization length, can be calculated by [52,55,56]

$$
\gamma = -\lim_{N \to \infty} \frac{1}{N} \ln \left| \frac{u_A^N}{u_A^1} \right|
$$
$$
= -\lim_{N \to \infty} \frac{1}{N} \ln \left| \prod_{j=1}^{N-1} \frac{K_a}{K_b + \Delta \cos(2\pi Q[j+1] + \phi)} \right|
$$
$$
= \lim_{N \to \infty} \frac{1}{N} \left| \sum_{j=1}^{N-1} \ln \left| \frac{K_b + \Delta \cos(2\pi Q[j+1] + \phi)}{K_a} \right| \right|. \quad (17)
$$

According to Weyl's equidistribution theorem and properties of irrational rotations [57,58], a sequence $2\pi Q, 4\pi Q, 6\pi Q, \ldots$, mod 2π is uniformly distributed in the interval $(-\pi, \pi)$, where Q is an irrational number. So, the summation in Eq. (17) can be converted to an integral over the phase $\varphi \in [0, 2\pi]$,

$$
\gamma = \frac{1}{2\pi} \int_0^{2\pi} \ln \left| \frac{K_b + \Delta \cos \varphi}{K_a} \right| d\varphi, \quad (18)
$$

which can be evaluated as

$$
\gamma = \begin{cases} \ln \frac{K_b + \sqrt{K_b^2 - \Delta^2}}{2K_a}, & K_b > \Delta, \\ \ln \frac{\Delta}{2K_a}, & K_b < \Delta. \end{cases} \quad (19)
$$

The topological phase transition boundaries can then be computed by considering when the Lyapunov exponent goes to zero, which corresponds to a divergent localization length. Note that with an A-A periodicity incommensurate with that of the lattice, all information about the phase shift ϕ which can be initially present in the modulation is washed out by the integration over φ. This proves that the topological edge modes of such a system will remain insensitive to phase shifts in the modulation, so long as is incommensurate with the lattice. This is not necessarily the case if the modulation is commensurate, and we shall delve into this point a bit more deeply in the following subsection.

Regardless of this subtle point, this analytical result can be verified numerically by computing the localization length at the central frequency $\omega = \omega_0 = \sqrt{\frac{K_a + K_b + \Delta}{m}}$ using a transfer

matrix method [56] as a function of K_a and Δ. The transfer matrices $T^i(\omega)$ are derived from Eq. (12) and have the form

$$
\begin{bmatrix} u_{i+2} \\ u_{i+1} \end{bmatrix} = T^i(\omega) \begin{bmatrix} u_{i+1} \\ u_i \end{bmatrix},
$$
$$
T^i(\omega) = \begin{bmatrix} \frac{m\omega^2 - K_a - K_b - \Delta}{K_{i+2}} & -\frac{K_{i+1}}{K_{i+2}} \\ 1 & 0 \end{bmatrix}, \quad (20)
$$

where $i \in [1, 2N - 2]$ is the index of masses and springs from left to right, such that $u_A^1 = u_1$, $u_B^1 = u_2$, $u_A^2 = u_3$, and so on. It is important to notice that the first and the last springs of the system are $K_1 = K_b + \Delta \cos[2\pi Q + \phi]$ and $K_{2N+1} = K_b + \Delta \cos(2\pi Q[2N + 1] + \phi)$. So $K_2 = K_4 = K_6 = \cdots = K_{2N} = K_a$. Since the transfer matrices of this problem have dimension two, there exist only two Lyapunov exponents $\gamma_1 = -\gamma_2$ (this is true if the first and last springs are equal) [56]. The localization length is then $\Lambda = \frac{1}{|\lambda_1|} = \frac{1}{|\lambda_2|}$. The result for the analytical calculation is shown as a black line in Fig. 4 for $K_b = 2$, $m = 1$, and $\omega = \omega_0 = \sqrt{\frac{K_a + K_b + \Delta}{m}}$, where it is clear that the divergence of the localization length for when the gap closes indeed occurs at the boundary between topological phases for our model. Thus, this property is not exclusive of electronic models.

C. Topological characterization in the commensurate regime

Here we derive the phase transition boundary for topological transition in the commensurate case. In a previous work [24] we have pointed out the relationship between the 1D topological phase of the model with the number of Dirac cones observed in the 2D spectrum originating from its 2D superspace description. Here, we build on these previous results by making use of the connection between the mobility edge at zero energy and the critical points where the winding number changes values. In this manner, we completely analytically characterize the 1D topological phase transition boundary, or equivalently the number of Dirac cones in the superspace description of this model. We show that this result reduces to the one obtained in [24] in the limit of long modulation periodicities.

The starting point of this analysis is, again, Eq. (15). In the incommensurate case, the summation can be converted to an integral due to the properties of rotations by an irrational angle. In the commensurate case this transformation cannot be performed, but nevertheless some simplifications can be implemented. We start from Eq. (15) by replacing $Q = p/q$, where p and q are relatively prime integers,

$$
\gamma = -\lim_{N \to \infty} \frac{1}{N} \ln \left| \prod_{j=1}^{N-1} \frac{K_a}{K_b + \Delta \cos\left(2\pi \frac{p}{q}[j+1] + \phi\right)} \right|. \quad (21)
$$

Let us define, for simplicity, $\varphi_j^{(q)} = 2\pi p[j+1]/q$. Now, although we cannot convert this expression to an integral such as in the incommensurate case, the periodicity in q nonetheless restricts the number of different terms that appear in the product. Specifically, $j + 1$ will yield the same term in the product if $j + 1 \mod q = j + 1$. This means that the product can be restricted to q different terms, and each term will

appear $(N-1)/q$ times. The resulting product is

$$\gamma = - \lim_{N \to \infty} \frac{1}{N} \ln \left| \prod_{j=1}^{q} \left[\frac{K_a}{K_b + \Delta \cos\left(\varphi_j^{(q)} + \phi\right)} \right]^{(N-1)/q} \right|. \tag{22}$$

We can bring a factor $(N-1)/q$ outside the logarithm, and in the large-N limit approximate $N - 1 \approx N$ so that the dependence in N drops from the expression and the limit can also be dropped. We find

$$\gamma = \frac{1}{q} \ln \left| \prod_{j=1}^{q} \left[\frac{K_b + \Delta \cos\left(\varphi_j^{(q)} + \phi\right)}{K_a} \right] \right|. \tag{23}$$

Similarly to the incommensurate case, the 1D topological transition boundary can be found by considering the set of parameters where the Lyapunov exponent goes to zero. This is given, in the commensurate case, by the polynomial equation

$$K_a^q = e^{i\theta_q} \prod_{j=1}^{q} \left[K_b + \Delta \cos\left(\varphi_j^{(q)} + \phi\right) \right]. \tag{24}$$

This polynomial equation is of degree q and can be solved for any commensurate periodicity. $e^{i\theta_q}$ is an arbitrary global phase which must be chosen so that all relevant parameters K_a, K_b, and Δ are real. For small periodicity, i.e., in the limit $pN/q \ll 1$, we can send $p/q \to 0$, and recover the transition obtained analytically for the large-periodicity limit in [24]. This is simply the boundary

$$K_a = \pm[K_b + \Delta \cos(\phi)]. \tag{25}$$

We see that the possibility of manipulation of the 1D topological edge modes becomes very rich in the case of a commensurate modulation, since an additional dependence on the modulation shift ϕ appears, whereas in the incommensurate case it is washed out by the angular integral. Thus, by tuning both the A-A disorder strength as well as this shift, a rich landscape of topological phase diagrams can appear. An example of such a phase diagram as a function of Δ and ϕ is given in Figs. 5(a) and 5(b), respectively. In both situations, an initially topologically trivial system can be driven into a topological phase via the A-A disorder term by changing the value of the quasidisorder strength or merely the shift ϕ. The fact that the contributions from the product do not wash out the dependence in ϕ is showcased in the inset of Fig. 5(c), where inspecting the symmetry of the distribution of the angles φ_j^q makes it clear that changing ϕ will result in measurable effects in the topological phase diagram. This is illustrated by plotting the analytical result for phase transition boundary in panel (c) as well as directly via the computation of the averaged LTM in panel (a).

D. Localization properties, inverse participation ratio, and finite size scaling analysis

Localization properties can also be accessed analyzing the inverse participation ratio (IPR). The state IPR is defined as
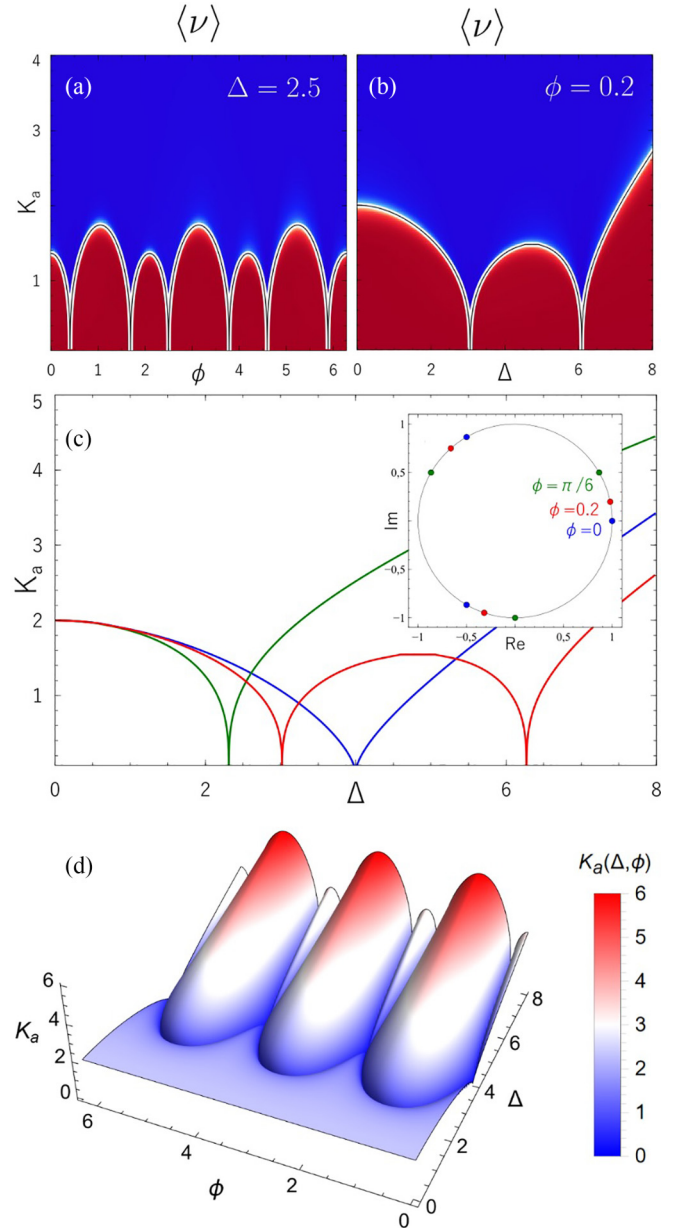
FIG. 5. (a) Averaged LTMs calculated for the spring-mass system with Aubry-André potential applied on the intercell spring constant in the case of a commensurate modulation of $Q = 1/3$ as a function of ϕ and K_a and for $K_b = 2$ and $\Delta = 2.5$. The blue region corresponds to the trivial phase with $\langle \nu \rangle = 0$ and the red region to the topological phase $\langle \nu \rangle = 1$. The white stripe indicates the region where the topological invariant did not converge to 0 or 1 due to the system's finite size, and the black line to the analytical result for the divergent localization length. (b) Similar phase diagram as a function of Δ and K_a. (c) Different topological transition boundaries as derived analytically from the divergent localization length. The inset shows, for each of the three phases $\phi = 0, 0.2, \pi/6$, the $q = 3$ angles $\varphi_j^{(q)}$ contributing to the product in Eq. (24). (d) Surface separating the topological and trivial phase in the parameter space spanned by K_a, Δ, and ϕ for $q = 3$. Panels (a) and (b) can be interpreted as phase diagrams with boundaries determined by sections of this surface along lines with fixed parameters $\Delta = 2.5$ and $\phi = 0.5$, respectively.
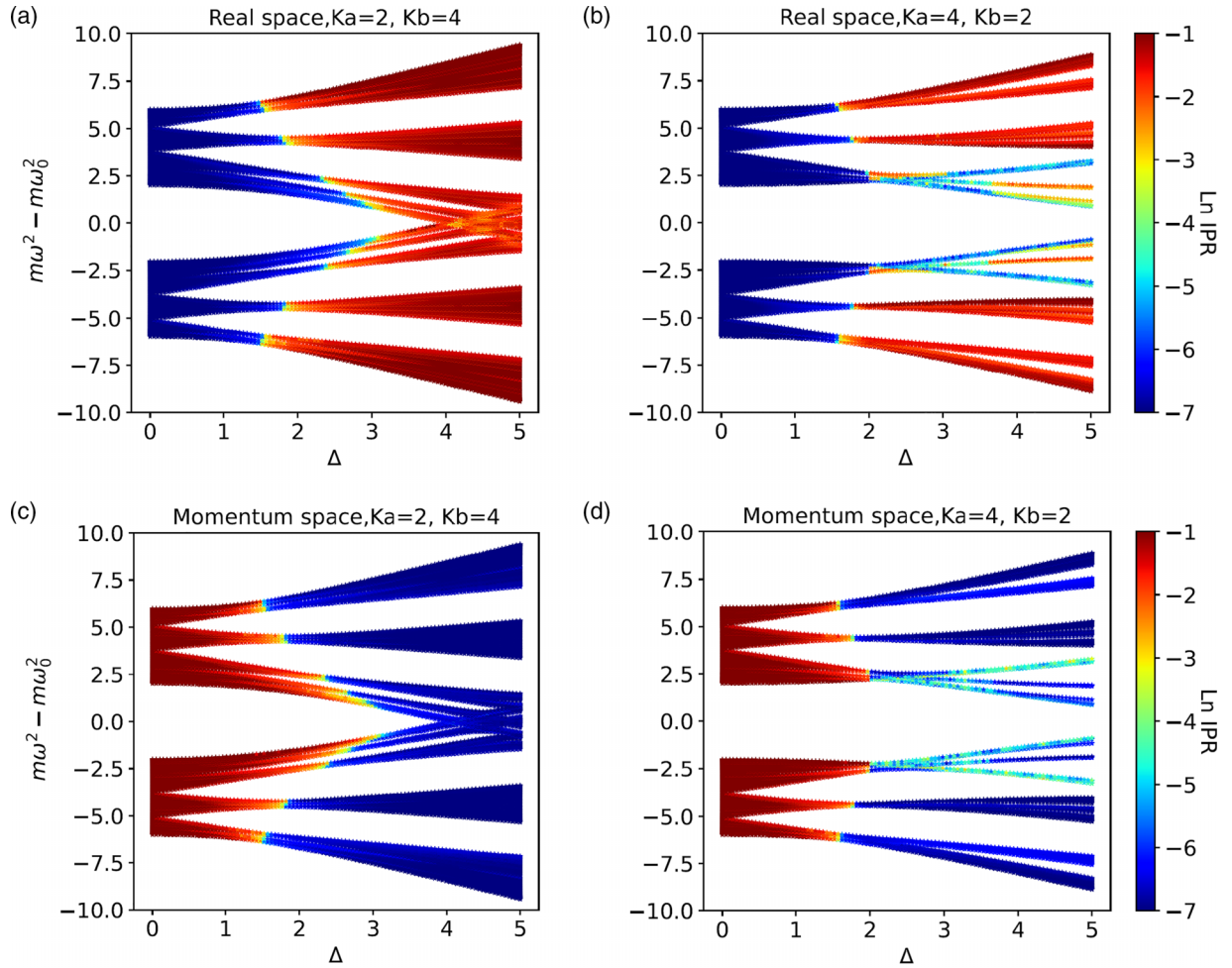
FIG. 6. ln(IPR) as a function of the eigenvalues ($m\omega^2 - m\omega_0^2$) for $N = 987$ unit cells, $\phi = 0$, $m = 1$, and (a) $K_b > K_a$ in real space; (b) $K_a > K_b$ in real space; (c) $K_b > K_a$ in momentum space; (d) $K_a > K_b$ in momentum space. In all cases, periodic boundary conditions were considered. If $K_b > K_a$, the transition between extended (localized) to localized (extended) phases in real (momentum) space is sharp, while for $K_a > K_b$ there are regions in which the transition is sharp and regions in which the state IPR does not converge to 1 (0). This could be an indication that the system is in the critical phase. However, in order to verify this statement, it is necessary to perform a finite size scaling analysis. See Figs. 7 and 8 and corresponding discussion in the main text.

[59–61]

$$\text{IPR}(|\psi\rangle) = \sum_{i=1}^{2N} |c_i|^4 \qquad (26)$$

given a normalized eigenstate $|\psi\rangle$ with dimension $2N$ and components c_i. If the eigenmode is an extended state, IPR $\simeq N^{-1}$. In the opposite scenario, if the eigenmode is perfectly localized, IPR $\simeq N^0 = 1$. Additionally, states are said to be in the critical phase if they are neither fully localized nor fully extended [26,34,61–63]. The states' IPR can be represented in a graph of the energy eigenvalues as a function of the Aubry-André potential strength Δ, with the lines colored by the value of the IPR of the corresponding eigenstate. Such representation allows us to visualize the transition between extended, localized, and critical phases, as shown in Fig. 6 for both real and momentum spaces. The transformation to momentum space is detailed in Appendix B.

When analyzing localization, one convenient quantity to compute is the fractal dimension Γ. This quantity is

independent of the system size and controls the asymptotic behavior of the system's IPR (defined as the average of all state IPRs and referred here as sIPR) with N according to the scaling law

$$\text{sIPR}(N) \sim (2N)^{-\Gamma}, \qquad (27)$$

in the limit $N \to \infty$. One way of accessing the value of Γ from the results for finite-size systems is via the introduction of the size-dependent quantity $D(N)$, that converges to Γ in the thermodynamic limit

$$\lim_{N \to \infty} D(N) = \Gamma, \qquad (28)$$

where $D(N)$ is defined as the average fractal dimension

$$D(N) = -\frac{\ln(\text{sIPR})}{\ln(2N)}, \qquad (29)$$

where $2N$ is the size of the system. For the extended phase, $\Gamma = 1$, and for the localized phase, $\Gamma = 0$. If $1 > \Gamma > 0$, the system is said to be critical [23,34]. Numerically, one can
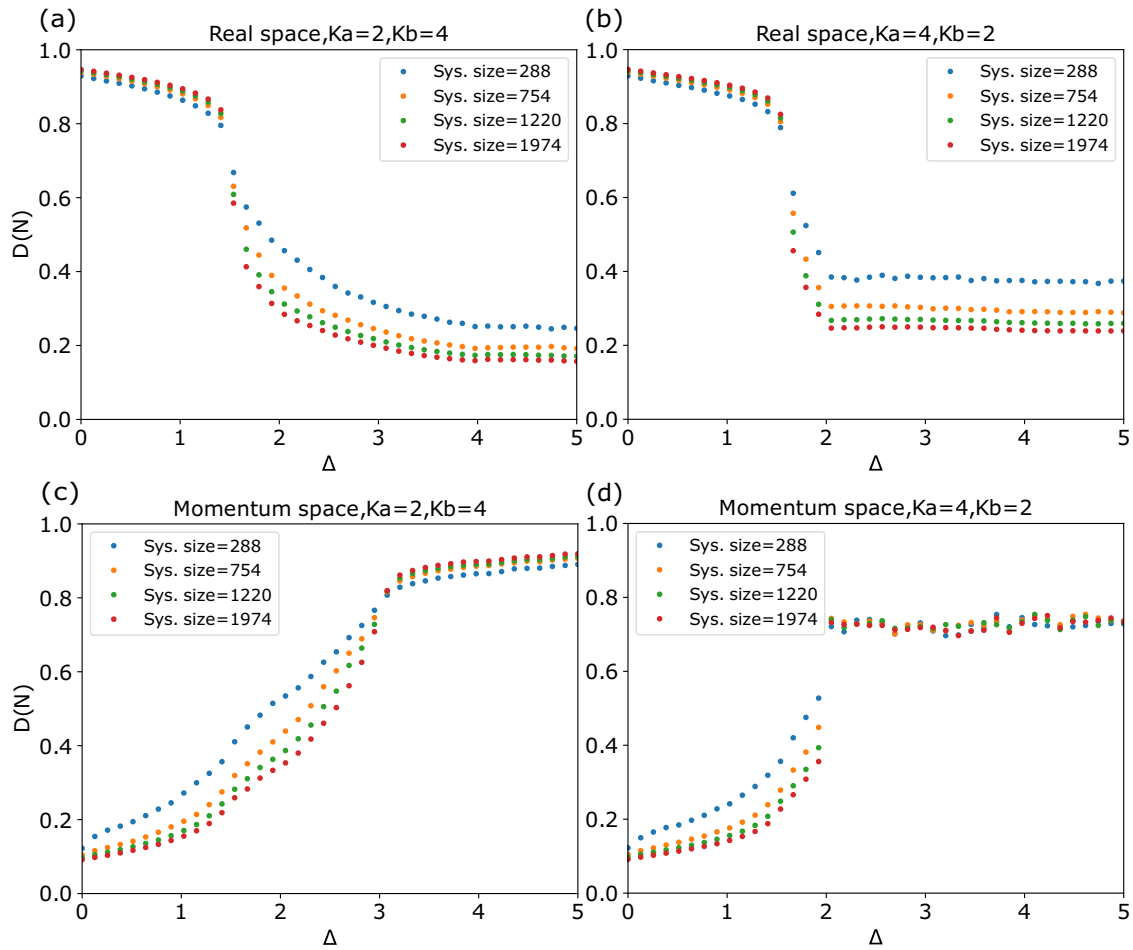
FIG. 7. Fractal dimension $D(N)$ as a function of Δ and the system size $2N$ for $\phi = 0$ and (a) $K_b > K_a$ in real space; (b) $K_a > K_b$ in real space; (c) $K_b > K_a$ in momentum space; (d) $K_a > K_b$ in momentum space. In cases (a) and (b) the system begins in an extended phase, since $D(N)$ approaches 1 with increasing N. Then, it transitions rather quickly to a localized phase as Δ increases, since $D(N)$ approaches 0 with increasing N. In (c) the system begins in a localized phase and transitions slowly to an extended phase. In (d) the behavior for $\Delta < 2$ is similar to case (c). After this point, however, the value of $D(N)$ is the same independently of N. This indicates that the system is indeed in the critical regime.

study the behavior of the quantity $D(N)$ that, for increasing N, approaches Γ. The advantage of computing $D(N)$ over computing only the IPRs or sIPR is that it gives a clear criterion for distinguishing between critical, extended, and localized phases, thus making it possible to predict the phase of the system in the thermodynamic limit. We then should expect that, for a given Δ, $D(N)$ converges to 1 with increasing N if the system is in an extended phase (all eigenstates are extended). On the contrary, $D(N)$ converges to 0 in the localized regime (where a finite fraction of the states are localized). If the system is in the critical regime, $D(N)$ assumes a finite value between 0 and 1 independent of N. For the cases depicted in Fig. 6 we compute $D(N)$ as a function of Δ and different system sizes, namely $N = 144, 377, 610$, and 987 unit cells. Results are shown in Fig. 7. In the real space, as seen in Figs. 7(a) and 7(b), the system seems to be in the extended phase for small Δ, since the greater the system size, the closer $D(N)$ is to 1. At around $\Delta = 1.5$, there is a transition to the localized phase, hinted at by the fact that $D(N)$ approaches 0 for increasing system sizes. This means that the critical states in Fig. 6(b) will become progressively localized for larger system sizes. In

momentum space, as seen in Figs. 7(c) and 7(d), the system begins localized for small Δ. In the case $K_a = 2, K_b = 4$, there is a transition to the extended phase close to $\Delta = 3$. Interestingly, for $K_a = 4, K_b = 2$, and $\Delta > 2$, the ratio $D(N)$ oscillates around a constant value between 0 and 1 independent of N. This is a strong evidence that the system tends to the critical phase in the thermodynamic limit.

Now, we can predict the fractal dimension Γ for a given Δ. We do so by plotting $-\ln(\text{sIPR})$ against $\ln(2N)$ for specific values of Δ and different system sizes. The resulting curve is linear, with slope $D(N)$, which, we stress, is the scaling exponent of the average sIPR. As N increases, the slope tends to $\Gamma = 1$ for the extended phase, $\Gamma = 0$ for the localized phase, and to $1 > \Gamma > 0$ for the critical phase. These curves are shown in Fig. 8 with the corresponding slope and confidence interval. For each case, we calculated $-\ln(\text{sIPR})$ for $\Delta = 1$ and $\Delta = 4$ and for $N = 233, 377, 610, 987, 1597, 2584, 4181, 6765$ unit cells. In Figs. 8(a) and 8(b) $\Delta = 1$ corresponds to the extended phase and $\Delta = 4$ to the localized phase, just as we would qualitatively expect from Figs. 7(a) and 7(b) [and from Figs. 6(a) and 6(b)]. We also expect that, if more points (corresponding
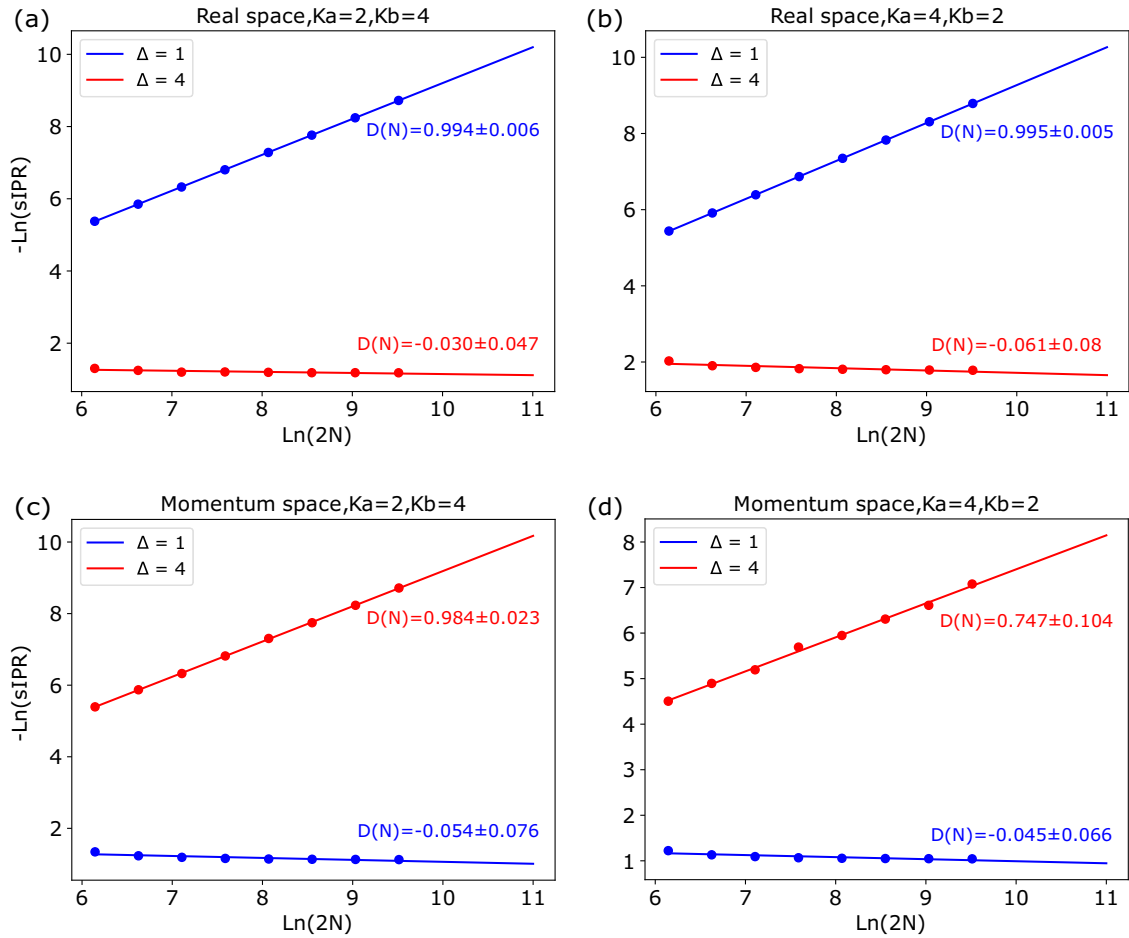
FIG. 8. Plot of $-\ln(\text{sIPR})$ versus $\ln(2N)$ for $\phi = 0$, $\Delta = 1$ (blue curves), $\Delta = 4$ (red curves), and for the following configurations: (a) $K_b > K_a$ in real space; (b) $K_a > K_b$ in real space; (c) $K_b > K_a$ in momentum space; (d) $K_a > K_b$ in momentum space. The slopes of the curves correspond to the quantity $D(N)$, a quantity that converges to the fractal dimension Γ in the thermodynamic limit. In cases (a) and (b) the blue curve indicates that for $\Delta = 1$ the system is in the extended phase and that for $\Delta = 4$ the system is in the localized phase. In case (c), $\Delta = 1$ corresponds to the localized phase and $\Delta = 4$ to the extended phase. The case (d) differs from the others in the sense that we have the value of $D(N)$ between 0 and 1 (see detailed discussion in the text).

to greater N) are added to the plot, the slope of the blue curve will become progressively closer to 1 and the slope of the red curve will become 0. In Fig. 8(c), $\Delta = 1$ corresponds to the localized phase and $\Delta = 4$ to the extended phase. In Fig. 8(d) the value for the slope of the red curve is in agreement with the result in Fig. 7(d), which shows that for $\Delta = 4$, the system average scaling dimension, with $D(N) \approx 0.75$, is dominated by the critical states. At first glace it may seem strange that the slopes of the red curves in Figs. 8(b) and 8(d) apparently lead to different conclusions for $\Delta = 4$, where we have $D(N) \approx 0$ in real space and $D(N) \approx 0.75$ in momentum space. This happens because of the same role played by the critical states in real space and in momentum space [see Figs. 6(b) and 6(d)]. In real space, and for $\Delta = 4$, we have the coexistence of localized and critical states [see Fig. 6(b)] and in momentum space, also for $\Delta = 4$, we have the coexistence of extended and critical states [see Fig. 6(d)]. The critical state IPR scales with $N^{-\Gamma_c}$ and $N^{-\Gamma_{c^k}}$ in real and momentum space, respectively, with $0 < \Gamma_c, \Gamma_{c^k} < 1$ [64,65]. Since extended and localized states scale with exponents $\Gamma = 1$ and $\Gamma = 0$, respectively, we

will have a finite $D(N) = \Gamma_{c^k}$ value in momentum space and $D(N) \approx 0$ in real space.

At last, one relevant question is whether there exists a correlation between topological and localized phases. To investigate this, we calculate an sIPR phase diagram for $K_a = [0, 4]$, $\Delta = [0, 5]$, $K_b = 2$, and $\phi = 0$ in real space. We know that, in real space, the system is in the extended state for small values of Δ, meaning all its states are extended. Then, the sIPR associated with these values of Δ will be 0. As Δ increases, the system can have extended and localized states coexisting, as shown in Fig. 6(a) for $\Delta = 2$, which would result in an sIPR > 0. Although the sIPR does not say which states are localized and which are extended, it provides information on whether the system has already transitioned from extended to localized (sIPR > 0) or whether all states are still extended (sIPR $= 0$). Thus, if sIPR > 0, the localization phase transition for at least some states has occurred. Thus, this allow us to separate the phase diagram between the fully extended phase (sIPR $= 0$) and nonextended phase (sIPR > 0). In Fig. 9 we compare this boundary with the topological one,
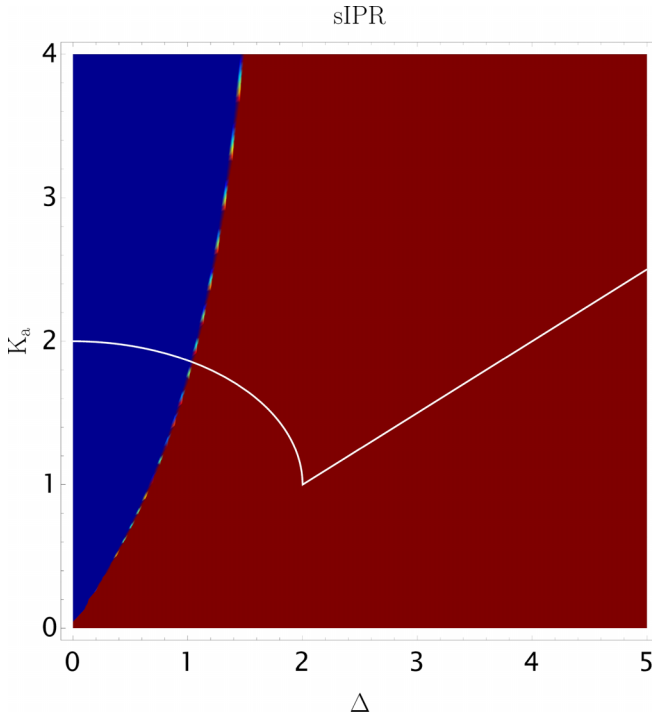
sIPR

FIG. 9. Averaged IPR calculated for the spring-mass system with Aubry-André modulation applied on the intercell spring constant for $K_b = 2$, $\phi = 0$, and $m = 1$. The blue region corresponds to the extended phase, in which all eigenstates of the system are extended and sIPR = 0. The red region corresponds to configurations for which some or all states have transitioned from extended to localized and thus sIPR > 0. The white line corresponds to the boundary between topological phases. Apparently, there exists no correlation between both phases.

as shown in Fig. 4, depicted in white. Above this line, the topological phase is trivial, and below it the nontrivial phase exists. The blue colored area of the phase diagram locates the extended phase (sIPR = 0) and the red colored area indicates that the phase transition has occurred for some or all states (sIPR > 0). We can see that there is no correlation between localization and topology in this model. Configurations of parameters K_a, K_b, and Δ that characterize a certain topological phase do not determine one specific localization phase. It is then possible, for example, to have the system in the extended phase and tune it to be either topological or trivial.

E. Calculation of the mobility edge

The mobility edge (ME) is another property of quasiperiodic models that is well known in the literature of electronic systems [23,27,28,66,67]. This property refers to the existence of a boundary separating extended from localized states. MEs exist in quasiperiodic one-dimensional systems, unlike in models subjected to Anderson disorder in one and two dimensions. Here we present an analytical derivation of MEs, which was previously thought not to be possible [68], based on Avila's global theory [50]. We note, however, that this derivation is only valid for the original, nonchiral version of our model, as in Eq. (10), setting $K_{0,j}^A = K_{0,j}^B = 0$. This is due to the fact that, in the chiral version, the imposed local spring removes the eigenvalue dependence in the diagonal of the dynamical matrix, making it impossible to obtain the localization length as a function of the eigenvalues $m\omega^2$ in analytical form (see, however, the methods used in Ref. [69]). To obtain the MEs analytically, we begin with the nonchiral equations of motion,

$$m\omega^2 u_A^j = [K_a + K_b + \Delta\cos(2\pi Q j + \phi)]u_A^j - K_a u_B^j - [K_b + \Delta\cos(2\pi Q j + \phi)]u_B^{j-1},$$

$$m\omega^2 u_B^j = \{K_a + K_b + \Delta\cos(2\pi Q[j+1] + \phi)\}u_B^j - K_a u_A^j - \{K_b + \Delta\cos(2\pi Q[j+1] + \phi)\}u_A^{j+1}, \tag{30}$$

where $j \in [1, N]$ is the unit cell index. Then, we isolate u_B^j and u_B^{j-1} as a function of u_A^j and u_A^{j+1},

$$u_B^j = \frac{K_a u_A^j + \{K_b + \Delta\cos(2\pi Q[j+1] + \phi)\}u_A^{j+1}}{K_a + K_b - m\omega^2 + \Delta\cos(2\pi Q[j+1] + \phi)}, \qquad u_B^{j-1} = \frac{K_a u_A^{j-1} + [K_b + \Delta\cos(2\pi Q j + \phi)]u_A^j}{K_a + K_b - m\omega^2 + \Delta\cos(2\pi Q j + \phi)}. \tag{31}$$

For cleaner notation, we define $Z = m\omega^2 - K_a - K_b$ and $f_j = \Delta\cos(2\pi Q j + \phi)$. Substituting u_B^j and u_B^{j-1} in the equation for u_A^j, we obtain

$$m\omega^2 u_A^j = (K_a + K_b + f_j)u_A^j - K_a\left(\frac{K_a u_A^j + (K_b + f_{j+1})u_A^{j+1}}{f_{j+1} - Z}\right) - (K_b + f_j)\left(\frac{K_a u_A^{j-1} + (K_b + f_j)u_A^j}{f_j - Z}\right). \tag{32}$$

Rearranging terms it is easy to see that

$$u_A^{j+1} = \frac{(Z - f_j)^2(Z - f_{j+1}) - K_a^2(Z - f_j) - (K_b + f_j)^2(Z - f_{j+1})}{K_a(K_b + f_{j+1})(Z - f_j)}u_A^j - \frac{K_a(K_b + f_j)(Z - f_{j+1})}{K_a(K_b + f_{j+1})(Z - f_j)}u_A^{j-1}. \tag{33}$$

Now, with Eq. (33) we can define a transfer matrix T^j as

$$\begin{bmatrix} u_A^{j+1} \\ u_A^j \end{bmatrix} = T^j \begin{bmatrix} u_A^j \\ u_A^{j-1} \end{bmatrix}, \qquad T^j(\omega, \phi) = \begin{bmatrix} \frac{(Z - f_j)^2(Z - f_{j+1}) - K_a^2(Z - f_j) - (K_b + f_j)^2(Z - f_{j+1})}{K_a(K_b + f_{j+1})(Z - f_j)} & -\frac{K_a(K_b + f_j)(Z - f_{j+1})}{K_a(K_b + f_{j+1})(Z - f_j)} \\ 1 & 0 \end{bmatrix}. \tag{34}$$

The maximal Lyapunov exponent $\gamma(\omega)$ can be calculated by computing the limit [70]

$$\gamma(\omega) = \lim_{N \to \infty} \frac{1}{N} \ln \left\| \prod_{j=1}^{N} T^j \right\|_2, \tag{35}$$

where $\ln \|M\|_2$ denotes the natural logarithm of the spectral radius of the matrix M, i.e., the maximum of the absolute values of its eigenvalues [70]. We proceed by writing T^j as a product,

$$T^j(\omega, \phi) = A^j(\omega, \phi) B^j(\omega, \phi), \quad A^j(\omega, \phi) = \frac{K_a^2}{K_a(K_b + f_{j+1})},$$

$$B^j(\omega, \phi) = \begin{bmatrix} \frac{(Z-f_j)^2(Z-f_{j+1}) - K_a^2(Z-f_j) - (K_b+f_j)^2(Z-f_{j+1})}{K_a^2(Z-f_j)} & -\frac{K_a(K_b+f_j)(Z-f_{j+1})}{K_a^2(Z-f_j)} \\ \frac{K_a(K_b+f_{j+1})}{K_a^2} & 0 \end{bmatrix}. \tag{36}$$

Note that all terms must be dimensionless, a multiplication by K_a^2 is required in A^j, and a division by K_a^2 is required in B^j. Using these elements, we seek to calculate the Lyapunov exponent: $\gamma(\omega) = \gamma_A(\omega) + \gamma_B(\omega)$, where

$$\gamma_A(\omega) = \lim_{N \to \infty} \frac{1}{N} \ln \prod_{j=1}^{N} \frac{K_a^2}{|K_a\{K_b + \Delta\cos(2\pi Q[j+1] + \phi)\}|},$$

$$\gamma_B(\omega) = \lim_{N \to \infty} \frac{1}{N} \ln \left\| \prod_{j=1}^{N} B^j(\omega, \phi) \right\|_2. \tag{37}$$

For $\gamma_A(\omega)$ we apply ergodic theory, as usual in this type of calculation [23,67]. This allows us to write $\gamma_A(\omega)$ as an integral over the phase φ:

$$\gamma_A(\omega) = \frac{1}{2\pi} \int_0^{2\pi} \ln \left| \frac{K_a^2}{K_a[K_b + \Delta\cos(\varphi)]} \right| d\varphi$$

$$= \begin{cases} -\ln\left(\frac{K_b + \sqrt{K_b^2 - \Delta^2}}{2K_a}\right), & K_b > \Delta, \\ -\ln\left(\frac{\Delta}{2K_a}\right), & K_b < \Delta. \end{cases} \tag{38}$$

As for $\gamma_B(\omega)$, we start by complexifying the phase of the cosine terms in $B^j(\omega, \phi)$: $\Delta\cos(2\pi Qj + \phi) \to \Delta\cos(2\pi Qj + \phi + i\epsilon)$. As $\epsilon \to \infty$, $f_j(\epsilon) = \Delta\cos(2\pi Qj + \phi + i\epsilon) \to \frac{\Delta}{2}e^{-(2\pi iQj + i\phi)}e^{\epsilon}$, since the exponential proportional to $e^{-\epsilon}$ vanishes. In this scenario it is easy to see that

$$\frac{Z - f_{j+1}(\epsilon)}{Z - f_j(\epsilon)} \xrightarrow{\epsilon \to \infty} \frac{\frac{\Delta}{2}e^{-(2\pi iQ[j+1]+i\phi)}e^{\epsilon}}{\frac{\Delta}{2}e^{-(2\pi iQj+i\phi)}e^{\epsilon}} = e^{-2\pi iQ}. \tag{39}$$

Then, the matrix $B^j(\omega, \phi, \epsilon)$ becomes

$$B^j(\omega, \phi, \epsilon)$$
$$= \begin{bmatrix} \frac{[Z-f_j(\epsilon)]^2 e^{-2\pi iQ} - K_a^2 - [K_b+f_j(\epsilon)]^2 e^{-2\pi iQ}}{K_a^2} & -\frac{[K_b+f_j(\epsilon)]e^{-2\pi iQ}}{K_a} \\ \frac{K_b+f_{j+1}(\epsilon)}{K_a} & 0 \end{bmatrix}. \tag{40}$$

Working with each term explicitly, substituting $Z = m\omega^2 - K_a - K_b$, $f_j(\epsilon) = \frac{\Delta}{2}e^{-(2\pi iQj+i\phi)}e^{\epsilon}$, and keeping only the highest power in ϵ,

$$B^j(\omega, \phi, \epsilon) = e^{-(2\pi iQ[j+1]+i\phi)}e^{\epsilon} \begin{bmatrix} \frac{-\Delta(m\omega^2 - K_a)}{K_a^2} & -\frac{\Delta}{2K_a} \\ \frac{\Delta}{2K_a} & 0 \end{bmatrix}. \tag{41}$$

The Lyapunov exponent $\gamma_B(\omega, \epsilon)$ is the natural logarithm of the spectral norm of $B^j(\omega, \phi, \epsilon)$,

$$\gamma_B(\omega, \epsilon) = \ln \|B^j(\omega, \phi, \epsilon)\|_2$$

$$= \epsilon + \ln \left| \frac{\Delta\left(K_a - m\omega^2 + \sqrt{m\omega^2(m\omega^2 - 2K_a)}\right)}{2K_a^2} \right|. \tag{42}$$

By the global theory [50], $\gamma_B(\omega) = \ln \left| \frac{\Delta(K_a - m\omega^2 + \sqrt{m\omega^2(m\omega^2 - 2K_a)})}{2K_a^2} \right|$. Then, the Lyapunov exponent is

$$\gamma(\omega) = \begin{cases} \ln \left| \frac{\Delta(K_a - m\omega^2 + \sqrt{m\omega^2(m\omega^2 - 2K_a)})}{K_a(K_b + \sqrt{K_b^2 - \Delta^2})} \right|, & K_b > \Delta, \\ \ln \left| \frac{(K_a - m\omega^2 + \sqrt{m\omega^2(m\omega^2 - 2K_a)})}{K_a} \right|, & K_b < \Delta. \end{cases} \tag{43}$$

At the MEs, the localization length Λ diverges [67]. Since $\Lambda = \gamma^{-1}(\omega)$, the condition for obtaining the MEs is $\gamma(\omega) = 0$. Thus, solving for $m\omega^2$ yields

$$m\omega^2 = \begin{cases} \frac{K_a(K_b + \Delta)}{\Delta}, & K_b > \Delta, \\ 2K_a, & K_b < \Delta. \end{cases} \tag{44}$$

In Fig. 10 we match our analytical results with the diagram of ln(IPR) as a function of Δ and $m\omega^2$. The diagram was calculated for a chain with 987 unit cells. One interesting property of this model is that all three localization regimes coexist within very well defined boundaries. For all cases studied, we note that above the mobility edge curve (pink curve in Fig. 10) all eigenstates are localized; below the curve, if $\Delta < K_b$, all states are extended, and if $\Delta > K_b$, all states are critical. Furthermore, critical states are always located below the threshold value $m\omega^2 = 2K_a$, such that the rectangle defined by $\Delta > K_b$, $m\omega^2 = 2K_a$ always predicts the location of critical eigenmodes.
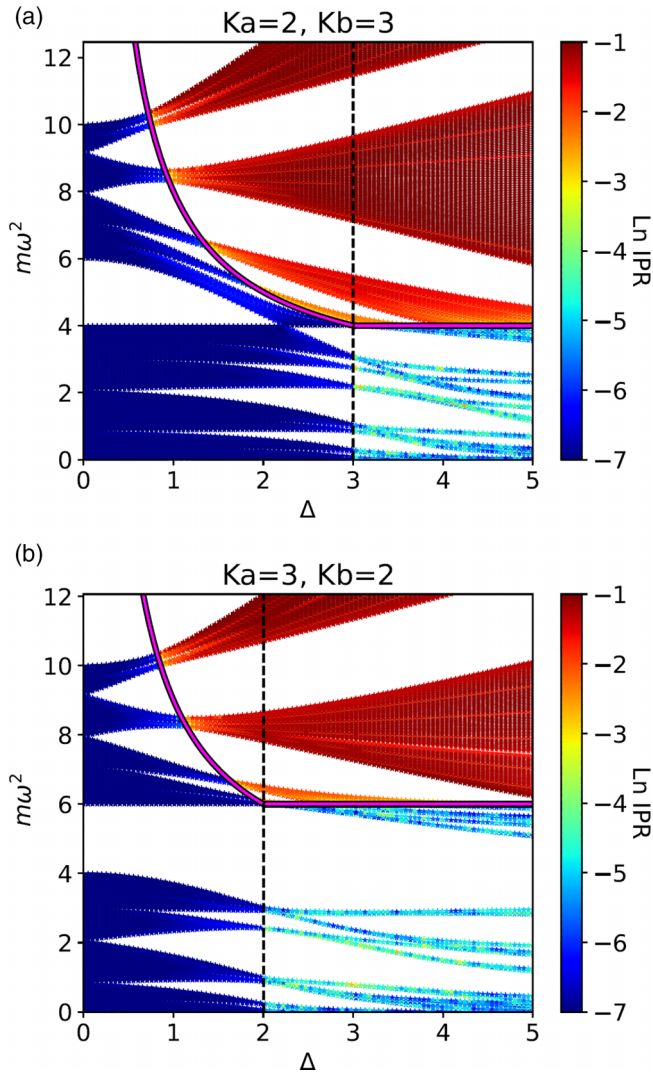
FIG. 10. ln(IPR) as a function of the eigenvalues $m\omega^2$ for the nonchiral version of our model for $N = 987$ unit cells, $\phi = 0$, $m = 1$ and (a) $K_b > K_a$, (b) $K_a > K_b$. The pink line is the result of our analytical calculation and precisely predicts the border between localized and nonlocalized eigenmodes. The black dashed line corresponds to $\Delta = K_b$. To the left of this dashed line, the MEs correspond to $m\omega^2 = \frac{K_a(K_b+\Delta)}{\Delta}$ and to the right of it, to $m\omega^2 = 2K_a$.

IV. FINAL REMARKS

In this work we studied topological transitions and localization properties of a mechanical SSH model with intercell spring constants subjected to an Aubry-André modulation. We applied an additional local spring on each mass to ensure chiral symmetry and used a topological invariant obtained from the real-space eigenmodes to understand and visualize the topological phases. An analytical computation of the Lyapunov exponents allowed us to predict for which values of the spring constants K_a, K_b and Aubry-André amplitude Δ the 1D topological phase transitions occur. The analytical result confirmed the numerical calculation of the boundary between phases. Additionally, with a detailed analysis in both real and momentum spaces using the state IPRs, we were able to associate each eigenmode of the chiral version of

our model with a given localization regime as a function of Δ, showing that it supports extended, localized, and critical states. Also, averaging all state IPRs and computing the fractal dimension $D(N)$ allows us to study the localization properties of the system as a whole and perform consistent finite scaling analysis of quasiperiodic models.

As for the nonchiral version of our model, we calculated the mobility edges analytically for a SSH-based system, perfectly predicting the border between localized and nonlocalized (either extended or critical) eigenstates. However, because of the rectangular boundaries bounding the critical phase, the system can only present the coexistence of extended and localized states or, alternatively, critical and localized states. We also observe that, for this model, it is possible to consistently predict the localization regime of each eigenstate based solely on the value of the tunable parameters K_a, K_b, and Δ. Our results extend what is known in quantum electronic topological systems and quantum electronic localization theory to the classical realm.

APPENDIX A: PERIODIC BOUNDARY CONDITIONS AND RATIONAL APPROXIMANTS

As stated in the main text, true quasiperiodicity can only be achieved in infinite systems. For finite size scaling analysis, we impose periodic boundary conditions to mimic an infinite system. This also allows us to perform transformations between real and momentum spaces. PBCs require the first and last spring constant to be equal (ϕ was set to 0 in this derivation for simplicity),

$$K_b + \Delta\cos(2\pi Q) = K_b + \Delta\cos(2\pi Q[N + 1]). \quad \text{(A1)}$$

If the the Aubry-André potential carried a truly irrational Q, this condition would never be satisfied because the cosine would never repeat itself. Then, it is clear that we need a rational approximant of Q, defined in such a way that Eq. (A1) is satisfied. The inverse of the golden ratio can be approximated by dividing two consecutive numbers of the Fibonacci sequence: $\tilde{Q} = \frac{F_{n-1}}{F_n}$, where $\tilde{Q}$ is the rational approximant such that the greater the index n, the closer $\tilde{Q}$ is from Q. Now, we can expand the cosine on the right-hand side of Eq. (A1) and

try to find a condition for $\tilde{Q}$,

$$
\cos(2\pi\tilde{Q}[N+1]) = \cos(2\pi\tilde{Q}N)\cos(2\pi\tilde{Q})
$$
$$
- \sin(2\pi\tilde{Q}N)\sin(2\pi\tilde{Q}). \quad \text{(A2)}
$$

Now, any choice of the type $\tilde{Q} = \frac{F_{n-1}}{F_n} = \frac{qs}{2N}$, $s = 1, 2, 3, \ldots$, $qs \in \mathbb{Z}$, makes the term $\sin(2\pi\tilde{Q}N)$ vanish ($\tilde{Q}N$ becomes an integer). This means that, to obey $\cos(2\pi\tilde{Q}) = \cos(2\pi\tilde{Q})$, we have to choose a rational approximant whose denominator F_n is related to the size of the system. The constants s and q are still to be determined though. Proceeding, we have

$$
1 = \cos(2\pi\tilde{Q}N) = \cos\left(2\pi\left[\frac{qs}{2N}\right]N\right) = \cos(\pi qs). \quad \text{(A3)}
$$

Naturally, quasiperiodicity requires no repetition of the cosine arguments throughout the chain. Because of this we need the smallest value of $\tilde{Q}$ that satisfies Eq. (A3). If $s = 1$, some approximants with odd numerator (F_{n-1}) would result in $1 = \cos(\pi q)$, which is false. Then, we need $s = 2$ such that, independent of the Fibonacci numbers chosen, we get a cosine equal to 1,

$$
\cos(2\pi\tilde{Q}N) = \cos\left(2\pi\left[\frac{qs}{2N}\right]N\right)\big\lfloor_{s=2} = \cos(2\pi q) = 1. \quad \text{(A4)}
$$

This means that the rational approximant of choice has to be $\tilde{Q} = \frac{F_{n-1}}{F_n} = \frac{q}{N}$, where N is the number of unit cells in the system and q its predecessor in the Fibonacci sequence. Thus, the size of the system is determined by the rational approximant chosen and vice versa. Finally, the dynamical matrix for the PBC system with off-diagonal A-A modulation is

$$
\mathbb{M} = \begin{bmatrix} K_a + K_b + \Delta & -K_a & 0 & \ldots & -(K_b + \Delta\cos[2\pi Q + \phi]) \\ -K_a & K_a + K_b + \Delta & -(K_b + \Delta\cos[4\pi Q + \phi]) & \ldots & 0 \\ 0 & -(K_b + \Delta\cos[4\pi Q + \phi]) & K_a + K_b + \Delta & \ldots & 0 \\ \ldots & \ldots & \ldots & \ldots & -K_a \\ -(K_b + \Delta\cos[2\pi Q + \phi]) & 0 & 0 & \ldots & K_a + K_b + \Delta \end{bmatrix}_{2N \times 2N}.
$$
$$(A5)$$

APPENDIX B: TRANSFORMATION TO MOMENTUM SPACE FOR HOPPING-MODULATED SSH-BASED QUASIPERIODIC SYSTEMS

Our goal in this section is to transform the equations

$$
m\omega^2 u_A^j = (K_a + K_b + \Delta)u_A^j - K_a u_B^j - [K_b + \Delta\cos(2\pi Qj)]u_B^{j-1},
$$
$$
m\omega^2 u_B^j = (K_a + K_b + \Delta)u_B^j - K_a u_A^j - \{K_b + \Delta\cos(2\pi Q[j+1])\}u_A^{j+1} \quad \text{(B1)}
$$

to momentum space. We begin by introducing the transformation

$$
u_\alpha^j = \sum_k e^{2\pi i Qkj}\psi_\alpha^k, \quad \text{(B2)}
$$

where $j \in [1, N]$ is the unit cell index in real space and $k \in [1, N]$ is the unit cell index in momentum space. α can be A, B, depending on the sublattice type.

1. Type-A mass equation

We begin by transforming the equation for the A sublattice, inserting Eq. (B2) for $\alpha = A$,

$$
m\omega^2 u_A^j = (K_a + K_b + \Delta)u_A^j - K_a u_B^j - [K_b + \Delta\cos(2\pi Qj)]u_B^{j-1}, \quad \text{(B3)}
$$

$$
m\omega^2 \sum_k e^{2\pi i Qkj}\psi_A^k = (K_a + K_b + \Delta)\sum_k e^{2\pi i Qkj}\psi_A^k - K_a \sum_k e^{2\pi i Qkj}\psi_B^k - [K_b + \Delta\cos(2\pi Qj)]\sum_k e^{2\pi i Qk(j-1)}\psi_B^k \quad \text{(B4)}
$$

$$
= (K_a + K_b + \Delta)\sum_k e^{2\pi i Qkj}\psi_A^k - \sum_k(K_a + K_b e^{-2\pi i Qk})e^{2\pi i Qkj}\psi_B^k - \Delta\cos(2\pi Qj)\sum_k e^{2\pi i Qk(j-1)}\psi_B^k. \quad \text{(B5)}
$$

Writing the cosine as a sum of exponentials

$$
= (K_a + K_b + \Delta)\sum_k e^{2\pi i Qkj}\psi_A^k - \sum_k(K_a + K_b e^{-2\pi i Qk})e^{2\pi i Qkj}\psi_B^k - \frac{\Delta}{2}\sum_k e^{2\pi i Qj}e^{2\pi i Qk(j-1)}\psi_B^k - \frac{\Delta}{2}\sum_k e^{-2\pi i Qj}e^{2\pi i Qk(j-1)}\psi_B^k.
$$
$$(B6)$$

Now, we put $e^{2\pi iQj}$ in evidence in the last two terms,

$$= (K_a + K_b + \Delta) \sum_k e^{2\pi iQkj} \psi_A^k - \sum_k (K_a + K_b e^{-2\pi iQk}) e^{2\pi iQkj} \psi_B^k - \frac{\Delta}{2} \sum_k e^{2\pi iQj(k+1)} e^{-2\pi iQk} \psi_B^k$$

$$- \frac{\Delta}{2} \sum_k e^{2\pi iQj(k-1)} e^{-2\pi iQk} \psi_B^k. \tag{B7}$$

Since the system is closed, we can change the index of the summation. We then make the following transformations:

$$k + 1 \to k', \quad \sum_{k=1}^{N} \to \sum_{k'=0}^{N-1},$$

$$k - 1 \to k'', \quad \sum_{k=1}^{N} \to \sum_{k''=2}^{N+1}. \tag{B8}$$

But due to PBCs, the 0th cell is the last one and the $(N + 1)$th cell is the first one. Then, the summations over m' and m'' are equivalent to summations in m. Applying this reasoning we obtain

$$= (K_a + K_b + \Delta) \sum_k e^{2\pi iQkj} \psi_A^k - \sum_k (K_a + K_b e^{-2\pi iQk}) e^{2\pi iQkj} \psi_B^k - \frac{\Delta}{2} \sum_k e^{2\pi iQjk} e^{-2\pi iQ(k-1)} \psi_B^{k-1}$$

$$- \frac{\Delta}{2} \sum_k e^{2\pi iQjk} e^{-2\pi iQ(k+1)} \psi_B^{k+1}. \tag{B9}$$

Lastly, the terms of the sum that multiply $e^{2\pi iQkj}$ have to be equal. We then obtain the final result

$$m\omega^2 \psi_A^k = (K_a + K_b + \Delta) \psi_A^k - (K_a + K_b e^{-2\pi iQk}) \psi_B^k - \frac{\Delta}{2} e^{-2\pi iQ(k-1)} \psi_B^{k-1} - \frac{\Delta}{2} e^{-2\pi iQ(k+1)} \psi_B^{k+1}. \tag{B10}$$

This is the result for the type-A mass equation.

2. Type-B mass equation

For the B sublattice, inserting Eq. (B2) for $\alpha = B$,

$$m\omega^2 u_B^j = (K_a + K_b + \Delta) u_B^j - K_a u_A^j - \{K_b + \Delta\cos(2\pi Q[j+1])\} u_A^{j+1}, \tag{B11}$$

$$m\omega^2 \sum_k e^{2\pi iQkj} \psi_B^k = (K_a + K_b + \Delta) \sum_k e^{2\pi iQkj} \psi_B^k - K_a \sum_k e^{2\pi iQkj} \psi_A^k - \{K_b + \Delta\cos(2\pi Q[j+1])\} \sum_k e^{2\pi iQk(j+1)} \psi_A^k \tag{B12}$$

$$= (K_a + K_b + \Delta) \sum_k e^{2\pi iQkj} \psi_B^k - \sum_k (K_a + K_b e^{2\pi iQ}) e^{2\pi iQkj} \psi_A^k - \Delta\cos(2\pi Q[j+1]) \sum_k e^{2\pi iQk(j+1)} \psi_A^k. \tag{B13}$$

Expanding the cosine as the sum of two exponentials, we get

$$= (K_a + K_b + \Delta) \sum_k e^{2\pi iQkj} \psi_B^k - \sum_k (K_a + K_b e^{2\pi iQ}) e^{2\pi iQkj} \psi_A^k - \frac{\Delta}{2} \sum_k e^{2\pi iQ(j+1)} e^{2\pi iQk(j+1)} \psi_A^k$$

$$- \frac{\Delta}{2} \sum_k e^{-2\pi iQ(j+1)} e^{2\pi iQk(j+1)} \psi_A^k. \tag{B14}$$

Now, we group exponentials with j in the exponent

$$= (K_a + K_b + \Delta) \sum_k e^{2\pi iQkj} \psi_B^k - \sum_k (K_a + K_b e^{2\pi iQ}) e^{2\pi iQkj} \psi_A^k - \frac{\Delta}{2} \sum_k e^{2\pi iQj(k+1)} e^{2\pi iQ(k+1)} \psi_A^k$$

$$- \frac{\Delta}{2} \sum_k e^{2\pi iQj(k-1)} e^{2\pi iQ(k-1)} \psi_A^k. \tag{B15}$$

The change in the summation index is performed exactly as for the A-type equation,

$$= (K_a + K_b + \Delta) \sum_k e^{2\pi iQkj} \psi_B^k - \sum_k (K_a + K_b e^{2\pi iQ}) e^{2\pi iQkj} \psi_A^k - \frac{\Delta}{2} \sum_k e^{2\pi iQjk} e^{2\pi iQk} \psi_A^{k-1} - \frac{\Delta}{2} \sum_k e^{2\pi iQjk} e^{2\pi iQk} \psi_A^{k+1}. \tag{B16}$$

Lastly, the terms of the sum that multiply $e^{2\pi i Q k j}$ have to be equal,

$$m\omega^2 \psi_B^k = (K_a + K_b + \Delta)\psi_B^k - (K_a + K_b e^{2\pi i Q})\psi_A^k - \frac{\Delta}{2}e^{2\pi i Q k}\psi_A^{k-1} - \frac{\Delta}{2}e^{2\pi i Q k}\psi_A^{k+1}. \tag{B17}$$

We then obtain the final result,

$$m\omega^2 \psi_A^k = (K_a + K_b + \Delta)\psi_A^k - (K_a + K_b e^{-2\pi i Q k})\psi_B^k - \frac{\Delta}{2}e^{-2\pi i Q(k-1)}\psi_B^{k-1} - \frac{\Delta}{2}e^{-2\pi i Q(k+1)}\psi_B^{k+1},$$

$$m\omega^2 \psi_B^k = (K_a + K_b + \Delta)\psi_B^k - (K_a + K_b e^{2\pi i Q})\psi_A^k - \frac{\Delta}{2}e^{2\pi i Q k}\psi_A^{k-1} - \frac{\Delta}{2}e^{2\pi i Q k}\psi_A^{k+1}. \tag{B18}$$

With this set of equations, we can produce the diagrams in Fig. 6.

[1] P. W. Anderson, Phys. Rev. **109**, 1492 (1958).

[2] A. Lagendijk, B. Tiggelen, and D. Wiersma, Phys. Today **62**(8), 24 (2009).

[3] E. Abrahams, P. W. Anderson, D. C. Licciardello, and T. V. Ramakrishnan, Phys. Rev. Lett. **42**, 673 (1979).

[4] Y. Fu, E. J. König, J. H. Wilson, Y.-Z. Chou, and J. H. Pixley, npj Quantum Mater. **5**, 71 (2020).

[5] A. C. Gadelha, D. A. Ohlberg, C. Rabelo, E. G. Neto, T. L. Vasconcelos, J. L. Campos, J. S. Lemos, V. Ornelas, D. Miranda, R. Nadas *et al.*, Nature (London) **590**, 405 (2021).

[6] M. Gonçalves, H. Z. Olyaei, B. Amorim, R. Mondaini, P. Ribeiro, and E. V. Castro, 2D Mater. **9**, 011001 (2022).

[7] A. Uri, S. C. de la Barrera, M. T. Randeria, D. Rodan-Legrain, T. Devakul, P. J. Crowley, N. Paul, K. Watanabe, T. Taniguchi, R. Lifshitz *et al.*, Nature (London) **620**, 762 (2023).

[8] S. Aubry and G. André, Ann. Israel Phys. Soc. **3**, 133 (1980).

[9] G. A. Dominguez-Castro and R. Paredes, Eur. J. Phys. **40**, 045403 (2019).

[10] M. Z. Hasan and J. E. Moore, Annu. Rev. Condens. Matter Phys. **2**, 55 (2011).

[11] F. Mei, G. Chen, L. Tian, S.-L. Zhu, and S. Jia, Phys. Rev. A **98**, 012331 (2018).

[12] I. Timoshuk and Y. Makhlin, arXiv:2302.10101.

[13] R. Citro and M. Aidelsburger, Nat. Rev. Phys. **5**, 87 (2023).

[14] A. Stern, Annu. Rev. Condens. Matter Phys. **7**, 349 (2016).

[15] W. P. Su, J. R. Schrieffer, and A. J. Heeger, Phys. Rev. Lett. **42**, 1698 (1979).

[16] J. Asbóth, L. Oroszlány, and A. Pályi, *A Short Course on Topological Insulators: Band Structure and Edge States in One and Two Dimensions*, Lecture Notes in Physics (Springer International Publishing, Switzerland, 2016).

[17] S. Basu, *Condensed Matter Physics: A Modern Perspective* (Institute of Physics Publishing, Bristol, UK, 2022).

[18] E. G. Cinnirella, A. Nava, G. Campagnano, and D. Giuliano, Phys. Rev. B **109**, 035114 (2024).

[19] S. Ryu, A. P. Schnyder, A. Furusaki, and A. W. W. Ludwig, New J. Phys. **12**, 065010 (2010).

[20] H. C. Wu, L. Jin, and Z. Song, Phys. Rev. B **103**, 235110 (2021).

[21] X. Shi, I. Kiorpelidis, R. Chaunsali, V. Achilleos, G. Theocharis, and J. Yang, Phys. Rev. Res. **3**, 033012 (2021).

[22] A. Nava, G. Campagnano, P. Sodano, and D. Giuliano, Phys. Rev. B **107**, 035113 (2023).

[23] Z. Lu, Z. Xu, and Y. Zhang, Ann. Phys. (Berlin, Ger.) **534**, 2200203 (2022).

[24] T. Antão, D. Miranda, and N. Peres, arXiv:2401.03541.

[25] Q. Tang and Y. He, Chin. Phys. B **32**, 127202 (2023).

[26] S. Roy, T. Mishra, B. Tanatar, and S. Basu, Phys. Rev. Lett. **126**, 106803 (2021).

[27] J. Biddle and S. Das Sarma, Phys. Rev. Lett. **104**, 070601 (2010).

[28] S. Ganeshan, J. H. Pixley, and S. Das Sarma, Phys. Rev. Lett. **114**, 146601 (2015).

[29] M. Schreiber, S. S. Hodgman, P. Bordia, H. P. Lüschen, M. H. Fischer, R. Vosk, E. Altman, U. Schneider, and I. Bloch, Science **349**, 842 (2015).

[30] H. P. Lüschen, P. Bordia, S. Scherg, F. Alet, E. Altman, U. Schneider, and I. Bloch, Phys. Rev. Lett. **119**, 260401 (2017).

[31] G. Roati, C. D'Errico, L. Fallani, M. Fattori, C. Fort, M. Zaccanti, G. Modugno, M. Modugno, and M. Inguscio, Nature (London) **453**, 895 (2008).

[32] N. Mott, J. Phys. C **20**, 3075 (1987).

[33] R. Abou-Chacra, D. J. Thouless, and P. W. Anderson, J. Phys. C **6**, 1734 (1973).

[34] F. Evers and A. D. Mirlin, Rev. Mod. Phys. **80**, 1355 (2008).

[35] M. Gonçalves, B. Amorim, E. V. Castro, and P. Ribeiro, Phys. Rev. Lett. **131**, 186303 (2023).

[36] M. Gonçalves, B. Amorim, E. V. Castro, and P. Ribeiro, SciPost Phys. **13**, 046 (2022).

[37] R. Süsstrunk and S. D. Huber, Science **349**, 47 (2015).

[38] L. M. Nash, D. Kleckner, A. Read, V. Vitelli, A. M. Turner, and W. T. M. Irvine, Proc. Natl. Acad. Sci. USA **112**, 14495 (2015).

[39] J. Vila, R. K. Pal, and M. Ruzzene, Phys. Rev. B **96**, 134307 (2017).

[40] H. Chen, H. Nassar, A. N. Norris, G. K. Hu, and G. L. Huang, Phys. Rev. B **98**, 094302 (2018).

[41] H. Chen, H. Nassar, and G. L. Huang, J. Mech. Phys. Solids **117**, 22 (2018).

[42] Y. Gong, L. Guo, S. Wong, A. J. Bennett, and S. S. Oh, Sci. Rep. **11**, 1055 (2021).

[43] E. L. Pereira, H. Li, A. Blanco-Redondo, and J. L. Lado, Phys. Rev. Res. **6**, 023004 (2024).

[44] Z. Yang, F. Gao, X. Shi, X. Lin, Z. Gao, Y. Chong, and B. Zhang, Phys. Rev. Lett. **114**, 114301 (2015).

[45] C. He, X. Ni, H. Ge, X.-C. Sun, Y.-B. Chen, M.-H. Lu, X.-P. Liu, and Y.-F. Chen, Nat. Phys. **12**, 1124 (2016).

[46] G. Ma, M. Xiao, and C. T. Chan, Nat. Rev. Phys. **1**, 281 (2019).

[47] Q.-B. Zeng, S. Chen, and R. Lü, Phys. Rev. B **94**, 125408 (2016).

[48] M. Yahyavi, B. Hetényi, and B. Tanatar, Phys. Rev. B **100**, 064202 (2019).

[49] T.-T. Xu and J.-R. Li, Prog. Theor. Exp. Phys. **2023**, 043I01 (2023).

[50] A. Avila, Acta Mathematica **215**, 1 (2015).

[51] E. J. Meier, F. A. An, A. Dauphin, M. Maffei, P. Massignan, T. L. Hughes, and B. Gadway, Science **362**, 929 (2018).

[52] I. Mondragon-Shem, T. L. Hughes, J. Song, and E. Prodan, Phys. Rev. Lett. **113**, 046802 (2014).

[53] A. Altland, D. Bagrets, L. Fritz, A. Kamenev, and H. Schmiedt, Phys. Rev. Lett. **112**, 206602 (2014).

[54] S. N. Liu, G. Q. Zhang, L. Z. Tang, and D. W. Zhang, Phys. Lett. A **431**, 128004 (2022).

[55] S. Longhi, Opt. Lett. **45**, 4036 (2020).

[56] J. A. Scales and E. S. V. Vleck, J. Comput. Phys. **133**, 27 (1997).

[57] H. Weyl, Math. Ann. **77**, 313 (1916).

[58] G. H. Choe, Proc. R. Ir. Acad. Sect. A **93A**, 193 (1993).

[59] R. J. Bell, Rep. Prog. Phys. **35**, 1315 (1972).

[60] D. J. Thouless, Phys. Rep. **13**, 93 (1974).

[61] Y.-C. Zhang and Y.-Y. Zhang, Phys. Rev. B **105**, 174206 (2022).

[62] A. Saul, A. M. Llois, and M. Weissmann, J. Phys. C **21**, 2137 (1988).

[63] C. W. Duncan, Phys. Rev. B **109**, 014210 (2024).

[64] B. Kramer and A. MacKinnon, Rep. Prog. Phys. **56**, 1469 (1993).

[65] T. Lv, T.-C. Yi, L. Li, G. Sun, and W.-L. You, Phys. Rev. A **105**, 013315 (2022).

[66] Y. Wang, X. Xia, L. Zhang, H. Yao, S. Chen, J. You, Q. Zhou, and X.-J. Liu, Phys. Rev. Lett. **125**, 196604 (2020).

[67] Y. Wang, X. Xia, Y. Wang, Z. Zheng, and X.-J. Liu, Phys. Rev. B **103**, 174205 (2021).

[68] T. Liu, X. Xia, S. Longhi, and L. Sanchez-Palencia, SciPost Phys. **12**, 027 (2022).

[69] M. Gonçalves, B. Amorim, E. V. Castro, and P. Ribeiro, Phys. Rev. B **108**, L100201 (2023).

[70] M. Pollicott, Inventiones mathematicae **181**, 209 (2010).